Volume 4 | Number 21 | 7 June 2016 | Pages 7965–8480

Journal of Materials Chemistry A

Materials for energy and sustainability

www.rsc.org/MaterialsA

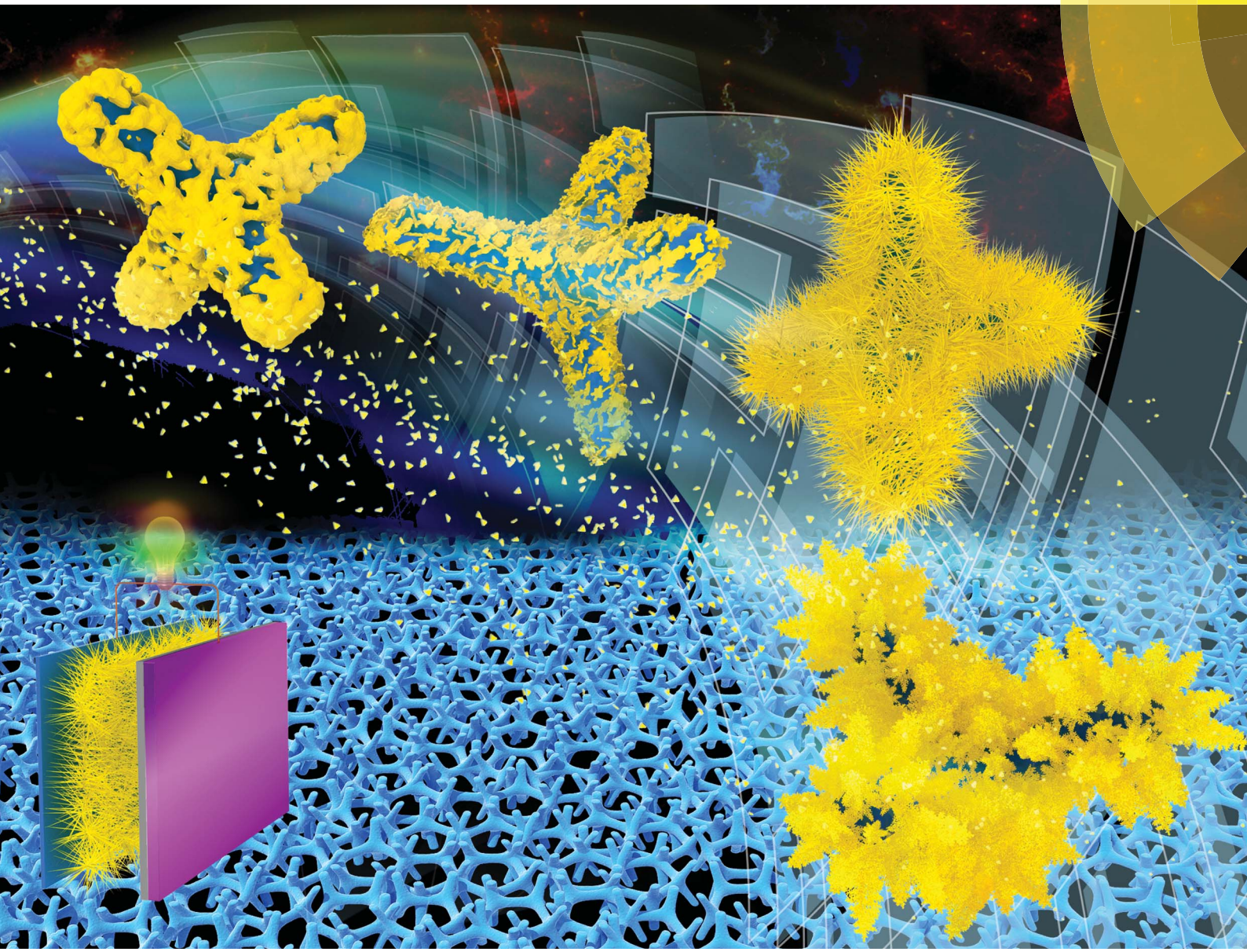

ISSN 2050-7488

ROYAL SOCIETY OF CHEMISTRY

PAPER

Heyou Han *et al.*

Regulating the oxidation degree of nickel foam: a smart strategy to controllably synthesize active Ni_3S_2 nanorod/nanowire arrays for high-performance supercapacitors

175 YEARS

Journal of Materials Chemistry A

PAPER

View Article Online
View Journal | View Issue

CrossMark click for updates

Cite this: J. Mater. Chem. A, 2016, 4, 8029

Regulating the oxidation degree of nickel foam: a smart strategy to controllably synthesize active Ni_3S_2 nanorod/nanowire arrays for high-performance supercapacitors†

Tingting Li,‡ Yunpeng Zuo,‡ Xiaomin Lei, Na Li, Jiawei Liu and Heyou Han*

A novel strategy is described in this study to construct three-dimensional (3D) nickel foam (NF) supported active Ni_3S_2 arrays with varieties of morphologies using a controllable pre-oxidation method followed by a post-hydrothermal treatment. A systematic study of the pre-oxidation effect is presented, and the possible reaction mechanism is discussed. Specifically, through accurately controlling the oxidation degree of the NF precursor, grass-like Ni_3S_2 nanorod/nanowire arrays grown *in situ* on the NF network are synthesized. Benefiting from the unique architecture to provide a large interfacial area, effective pathway for charge transport and high electrochemical activity from Ni_3S_2, the binder-free electrode exhibits remarkable electrochemical performances with a specific areal capacitance of 4.52 F cm^{-2} at 1.25 mA cm^{-2}, as well as superior cycling stability (108.3% capacitance retention after 2000 cycles). An aqueous asymmetric supercapacitor device composed of such an electrode as the positive electrode and nitrogen-doped porous graphitic carbon (NPGC) as the negative electrode achieves a high energy density of 48.5 W h kg^{-1} and power density of 4.8 kW kg^{-1}. Further, two such 4 cm^2 devices connected in series can successfully illuminate three color-changing LEDs for a long time, demonstrating the great potential for high-performance supercapacitors. The smart strategy described herein could be widely adopted to create other composites with desirable nanostructures.

Received 21st February 2016
Accepted 1st April 2016

DOI: 10.1039/c6ta01547f

www.rsc.org/MaterialsA

Published on 04 April 2016. Downloaded on 25/05/2016 13:06:36.

1. Introduction

Supercapacitors, known as electrochemical capacitors, are now attracting intensive attention because of their desirable properties including high power density, short charging times and long cycle life.[1–4] Currently, supercapacitors are mainly applied as rapid power delivery and recharging devices.[2,5] Due to the different charge-storage mechanisms, supercapacitors deliver relatively lower energy densities than batteries, which seriously hamper their large-scale applications.[6–8] In order to avoid this undesirable situation, it is extremely urgent to develop high performance supercapacitors with high energy densities while maintaining satisfactory power density and excellent cycling stability. An effective route for improving the energy density is to use an asymmetrical supercapacitor design or choose organic electrolytes to increase the operating voltage.[9,10] Another high-efficiency strategy used widely is to utilize redox-active electrode materials with unique morphology to afford high specific capacitance.[1,2]

In recent years, nanostructured nickel and cobalt oxides/sulfides/hydroxides have been extensively studied as pseudo-capacitance electrode materials due to their excellent intrinsic properties, such as high theoretical specific capacitance, low cost, and environment-friendly nature.[11–17] Among them, nickel sulfides have attracted increasing interest because of their numerous excellent performances, which make them quite suitable for various electrochemical applications, especially for supercapacitors.[16–22] However, as is well known, with the sluggish redox reaction kinetics and poor conductivity, the above-mentioned electroactive materials suffer from relatively low electrical energy density, poor capacity retention and even worse cycling stability when used as supercapacitor electrodes.[23] To address these problems, highly conductive materials (*e.g.* Au,[24] graphene,[7,25] conducting polymers[3,26]) are usually combined with pseudo-capacitive materials to enhance conductivity and stability by the synergistic effects between the two components. Nevertheless, the inferior charge storage and rate capability still limit further development and wide applications of these hybrids. Consequently, a key challenge in this direction is to build novel electrodes with well-suited architecture, in which fast ion and electron transfer is guaranteed.

State Key Laboratory of Agricultural Microbiology, College of Science, Huazhong Agricultural University, 1 Shizishan Street, Wuhan 430070, PR China. E-mail: hyhan@mail.hzau.edu.cn; Fax: +86-27-87288505; Tel: +86-27-87288505

† Electronic supplementary information (ESI) available. See DOI: 10.1039/c6ta01547f

‡ These authors contributed equally to this work.

Published on 04 April 2016. Downloaded on 25/05/2016 13:06:36.

To date, a smart design is widely adopted which relies on various 3D conductive matrixes to grow electroactive material arrays with well-defined morphologies. The innovative strategy can synergistically combine the merits of their constituent components in that conductive backbones not only possess high electrical conductivity but also supply good structural and mechanical stability to high-performance supercapacitors.[27–30] Among these, nickel foam (NF) is considered as the main candidate for loading various pseudo-capacitive materials due to the superior features of uniform macroporous structure, huge supporting area and high electrical conductivity. For instance, Ai *et al.*[31] reported a novel branched $CoMoO_4$@$CoNiO_2$ core/shell nanowire array on NF, which demonstrated a high specific areal capacitance (5.31 F cm^{-2} at 5 mA cm^{-2}) and superior cycling stability with 159% capacity retention after 5000 cycles. Huo *et al.*[18] synthesized 3D Ni_3S_2 nanosheet arrays grown on NF, which showed a specific capacitance of 1370.4 F g^{-1} at a current density of 2 A g^{-1}, good rate capability and cycling stability. Zhang *et al.*[32] successfully fabricated a novel Ni_3S_2 hierarchical dendrite framework using NF as the substrate. The electrode delivered a high capacitance of 710 F g^{-1} at 2 A g^{-1} with excellent capacitance retention of 621.6 F g^{-1} after 2000 cycles at a current density of 5 A g^{-1}. In particular, hierarchical nanowire and nanorod arrays vertically supported on 3D porous NF are the most advanced form used to construct supercapacitor electrodes due to their large surface area and fast electrical pathway for electron transport.[33,34] Previous studies for nickel sulfide arrays supported on NF showed that they are either unitary in morphology (*e.g.* nanosheets),[18,20] or require additives and toxic organic solvents to control the final morphology,[12,35] which limit their widespread practical application. To date, there is still lack of simple and high-efficiency methods to synthesize nickel sulfide arrays with precise structure control.

In the present work, we demonstrate an innovative and effective approach to design and fabricate hierarchical Ni_3S_2 grass-like nanorod/nanowire arrays on NF (NF-4-S) as a binder-free electrode for high-performance supercapacitors. Herein, NF first underwent a controllable pre-oxidation process, followed by a facile hydrothermal reaction. In addition to being the conductive frame to support active Ni_3S_2 arrays, the 3D NF also acted as the nickel source to form Ni_3S_2 crystals. This ingenious design enables wonderful electrical contact between the current collector and active material, thus can effectively improve ion and charge transportation. More significantly, through adjustment of the oxidation degree of the NF precursor, the final structure can be easily tuned with the morphological variation of nanoplates, nanorods/nanowires and flower-shaped hierarchical dendrites. This paper firstly verified if the pre-oxidation degree of NF can affect the morphology and electrochemical properties of the final product. Due to the unique structural features with a large accessible area, the optimal NF-4-S demonstrated superior electrochemical properties to other Ni_3S_2-based electrodes. Additionally, an as-prepared asymmetric supercapacitor, which consisted of an NF-4-S anode and a nitrogen-doped porous graphitic carbon (NPGC) cathode, exhibited high specific capacitance of 131.7 F g^{-1}, good rate capability, outstanding cycling stability, and remarkable energy density (48.5 W h kg^{-1} at a power density of 87.4 W kg^{-1}). These findings highlight the great application potential of NF-4-S for energy storage.

2. Experimental section

2.1 Fabrication of partially oxidized NF (NF-*x*)

NF (2 × 2 cm^2) was cleaned ultrasonically first with 2 M HCl solution in an ultrasound bath for 5 min, and then washed with deionized water and ethanol several times. After vacuum drying, the cleaned NF was calcined at 700 °C for 2 h with different N_2 flow rates (600 mL min^{-1}, 400 mL min^{-1}, 200 mL min^{-1} and 0 mL min^{-1}), which were labeled as NF-6, NF-4, NF-2 and NF-0, respectively.

2.2 Synthesis of Ni_3S_2 arrays supported on partially oxidized NF

The above obtained partially oxidized NF was immersed in a Teflon-lined stainless steel autoclave containing a 40 mL aqueous solution of 50 mg thioacetamide (TAA, C_2H_5NS). Then, the autoclave was sealed for hydrothermal reaction at 180 °C for 6 h. After cooling down to room temperature, the resulting samples were rinsed several times with deionized water and ethanol, and dried in vacuum at 60 °C for 10 h. Depending on the degree of oxidation, the sulfurized samples were referred to as NF-6-S, NF-4-S, NF-2-S and NF-0-S, respectively. For comparison, pure NF was also subjected to the hydrothermal treatment process under the same conditions without high temperature oxidation etching, which was denoted as NF-S.

2.3 Synthesis of NPGC

NPGC was synthesized based on the template method as described in our previous report.[36] Briefly, 31.5 g of melamine was added to a 50 mL formaldehyde solution under stirring, and the pH of the mixture was adjusted to 8–9 by adding dilute NaOH. When the solution became clear at 80 °C, dilute HCl was introduced to adjust the solution to pH 5–6. Subsequently, 60 g of hydrophilic nano-$CaCO_3$ was added with vigorous stirring. Over a 0.5 h period a gel-like mixture was prepared. The composites were left to vacuum dry at 60 °C overnight. Then, the material was directly carbonized at 900 °C for 2 h under N_2 flow. The template was removed by dilute HCl washing for 24 h. Finally, the resultant material was filtered and washed. After drying, the NPGC was obtained.

2.4 Characterization

Scanning electron microscopy (SEM) and energy dispersive X-ray spectrometry (EDS) analysis were carried out using a SU8010 field emission scanning electron microscope. Transmission electron microscopy (TEM) images and selected area electron diffraction (SAED) patterns were collected on a JEM-2010 with a microscope operating at 200 kV. X-ray diffraction (XRD) spectra were obtained using a Rigaku D/MAX-rA diffractometer with Cu Kα radiation (λ = 1.5406 Å). X-ray photoelectron spectra (XPS) were measured using a Thermo VG Multilab

 This journal is © The Royal Society of Chemistry 2016

Published on 04 April 2016. Downloaded on 25/05/2016 13:06:36.

2000 spectrometer equipped with a monochromatic Al Kα radiation source at room temperature.

2.5 Electrochemical measurements

Electrochemical analyses were performed using a conventional three-electrode system equipped with a saturated calomel electrode (SCE) as the reference electrode and platinum foil as the counter electrode at ambient temperature, respectively. The NF composite, that served as a binder-free electrode material, was directly used as the working electrode. The NPGC electrode was prepared by mixing electrode materials, acetylene black and polytetrafluoroethylene (60 wt%) in a mass ratio of 8 : 1 : 1 in isopropanol. The slurry of the mixture was then coated onto the NF current collectors. Finally, the as-fabricated electrode was left to dry in an oven at 80 °C for 24 h. The mass loading of the NPGC materials was about 5.0 mg cm^{-2}. The asymmetric supercapacitor was tested with the NF composite as the positive electrode and NPGC as the negative electrode, which were assembled together with one piece of cellulose paper separator sandwiched in between. The whole configuration was sealed using a PET membrane. All electrochemical measurements were carried out using a CHI 660D (Chenhua, Shanghai) electrochemical workstation in 3 M KOH aqueous solution. The mass per unit area of the active Ni_3S_2 arrays on NF was calculated depending on the weight difference before and after treatment of NF. It can be assumed that the mass increase of NF was due wholly to the introduction of sulfur. Based on this, the loading mass of active Ni_3S_2 for NF-4-S was calculated to be about 4.3 mg cm^{-2}. In fact, the actual mass of Ni_3S_2 is lower than the presented value.

Cyclic voltammetry (CV), galvanostatic charge–discharge (GCD) and electrochemical impedance spectroscopy (EIS) were employed to evaluate the electrochemical performances of electrodes. The specific areal capacitance in a three-electrode system is calculated according to the following equation: $C_s = I_s \times t/V$, where C_s (F cm^{-2}), I_s (A cm^{-2}), t (s), and V (V) represent the specific areal capacitance, current density, discharge time and discharge voltage range, respectively.[37] The specific capacitance of the asymmetric supercapacitor was calculated from GCD curves as follows: $C = I \times t/(V \times m)$, where m (g) is the total mass of the active material in the positive and negative electrodes and I (A) is the discharge current. The energy density (E) and power density (P) of the asymmetric supercapacitors are obtained from the following equations: $E = C \times V^2/(2 \times 3.6)$, $P = E \times 3600/t$.[23,28,29] EIS measurements were recorded at open circuit potential with an amplitude of 5 mV in the frequency ranges of 10 mHz to 100 kHz.

3. Results and discussion

3.1 Material characterization

NF first underwent a thermal annealing process to form NiO shells around the substrate. To get more insight into the effect of oxidation degree on controlling the morphology of the finally synthesized samples, we performed this operation with different nitrogen volumes. Fig. 1 gives the SEM images of NF-6, NF-4, NF-2 and NF-0. Different from the pristine NF with a smoother surface (Fig. S1†), an uneven NiO layer with a coarse and porous surface is observed for oxidized NF products through the high temperature annealing process (Fig. 1a–d). This is completely different from the low temperature heat treatment with a dense layer of NiO.[38] Magnified SEM observations clearly reveal that the surface of conductive NF became rough with major protuberance and sunken holes (Fig. 1e–h). The surface morphology looks much like a seriously etched reef and withered bark. Based on the above observation, a possible mechanism for the formation of the unsealed oxide layer can be proposed as follows: the molar volume of Ni (~6.6 cm^3 mol^{-1}) is smaller than that of NiO (~11.2 cm^3 mol^{-1}). This results in the growth of NiO continuously extending outwardly in the initial stage of oxidation.[39,40] The intercalation and adsorption of oxygen atoms is closely linked to the surface state of the NF skeleton. As the oxidation proceeds, the Kirkendall effect and strain at the interface could play predominant roles in causing the rough surface and additional pores in the skeleton areas due to the different interfacial diffusion rates of oxygen and nickel atoms.[41,42] On the other hand, due to the presence of nitrogen, only a fraction of the top layer of Ni was oxidized, leaving the remaining exposed active Ni for further reaction. More specifically, these irregular gullies and projections increased the contact area of the substrate surface with liquid ions, which promoted the adequacy and efficiency of subsequent reactions. Fig. 1i shows the XRD patterns of the pure NF and the corresponding samples (NF-6, NF-4, NF-2, NF-0) with different oxidation degrees. For pure NF, the XRD pattern proves the existence of three crystalline peaks at 2θ of 44.6°, 51.9° and 76.3°, respectively. After high temperature oxidation of NF, five new peaks at $2\theta = 37.4°$, 43.4°, 62.8°, 75.4° and 79.3° occurred, which are indexed as (111), (200), (220), (311) and (222) peaks from NiO (JCPDS no. 47-1049).[43,44] The coexistence of Ni peaks and NiO peaks in these samples indicates the partial oxidation of NF under high temperature treatment. Moreover, the intensity ratio of NiO peaks increased dramatically with the decrease of N_2 flow, suggesting that more metallic Ni was converted to NiO. Especially, NF-0 shows strong NiO peaks and weak metallic Ni peaks, suggesting that the sample experienced severe oxidation.

Sulfurized samples were obtained by a one-step hydrothermal process without any post-treatment. The original 3D porous architectures may result in a good mixture of remaining Ni and sulfur ions during the hydrothermal treatment process, thus leading to an excellent Ni-S initial contact, which will benefit the formation of Ni_3S_2. After interaction and oriented growth, well-defined Ni_3S_2 arrays directly supported on NF can be obtained. The microstructure of the as-prepared NF-4-S was first investigated by SEM. As shown in Fig. 2a, NF-4-S surface is fully covered by grass-like nanorods/nanowires to form a 3D hierarchical structure. The magnified SEM images further reveal that some nanowires extend based on nanorods axis. The rest grow directly from the attached substrate with a maximum diameter of ~300 nm (Fig. 2b and c). Fortunately, these nanowires and nanorods grow perpendicularly on the NF substrate and are separated adequately. The unique 3D hierarchical

Published on 04 April 2016. Downloaded on 25/05/2016 13:06:36.

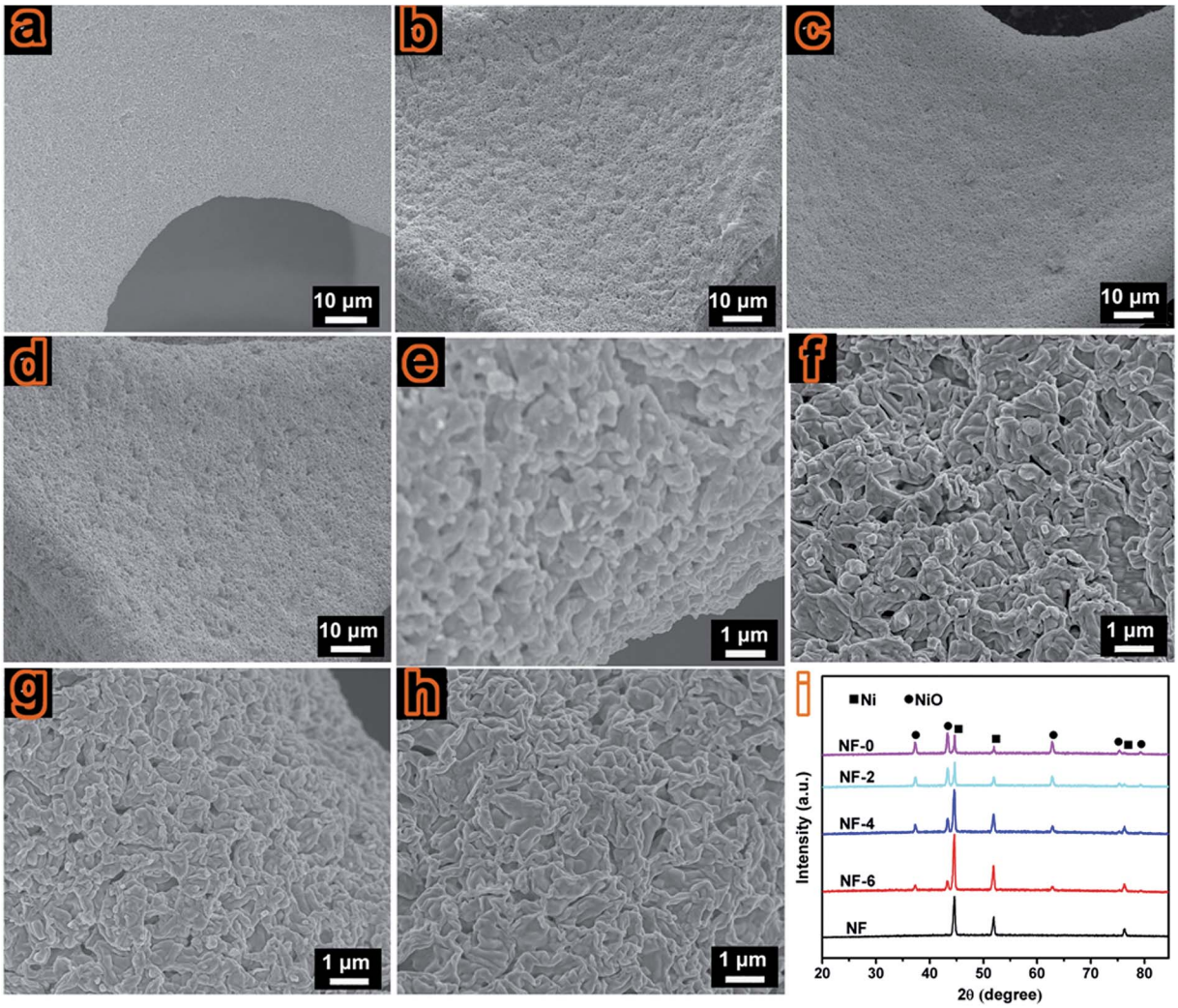

Fig. 1 Low-magnification SEM images of (a) NF-6, (b) NF-4, (c) NF-2, (d) NF-0 and high-magnification SEM images of (e) NF-6, (f) NF-4, (g) NF-2, (h) NF-0. (i) XRD patterns of pure NF and oxidized NF products.

structure would significantly facilitate electron transport and electrolyte ions accessibility to the surface of the active material, and enable a fast redox reaction.[31,37] Fig. 2d shows the representative TEM image of grass-like nanowires growing tightly on the inner NF backbones. The corresponding HRTEM image (Fig. 2d1) reveals clear lattice spacing of 0.28 nm indexed to the (110) crystal plane of Ni_3S_2.[23,32] The related electron diffraction spots (EDS) from fast Fourier transform (FFT) spectra demonstrate the single-crystal nature of the Ni_3S_2 nanowires, as shown in Fig. 2d2. In addition, scanning electron microscopic elemental mapping was employed to further investigate the elemental distribution of the NF-4-S sample. As shown in Fig. 2e–h, both Ni and S with strong signals are observed in the whole region, confirming the massive generation of the nickel sulfide nanostructure during the hydrothermal treatment. In addition to the backbone, it can be obviously found from the edge region that the distribution of S shows the clear outline of nanowires. In other words, active nickel sulfide constituted the vertically aligned array architecture. Additionally, only minor amounts of oxygen element were detected in the observed field, which were derived from previous oxidation. This can also be verified from the subsequent XRD and XPS results.

Fig. 3a presents the XRD patterns of as-prepared NF-0-S, NF-2-S, NF-4-S, NF-6-S and NF-S. Besides the characteristic peaks of Ni and NiO, a few new peaks located at $2\theta = 21.7$, 31.1, 37.8, 49.7 and 55.2° are also observed in the XRD pattern, which correspond to the single crystalline nature of Ni_3S_2 (JCPDS no. 44-1418).[35,45] No other impurity peak was detected, indicating the high purity of these samples. As expected, NF-S displayed the obvious characteristic diffraction peaks of Ni_3S_2, confirming the successful conversion from Ni to Ni_3S_2 by a sulfurization process. With increasing oxidation degree, the intensity of the Ni_3S_2 characteristic peaks gradually decreases, and the peaks at around 21.7°, 31.1° and 37.8° successively disappeared for NF-0-S, NF-2-S and NF-4-S. Especially for NF-0-S, only two very weak Ni_3S_2 peaks were observed at 49.7 and 55.2° owing to severe oxidation, indicating the low crystallization and small amount

 This journal is © The Royal Society of Chemistry 2016

Published on 04 April 2016. Downloaded on 25/05/2016 13:06:36.

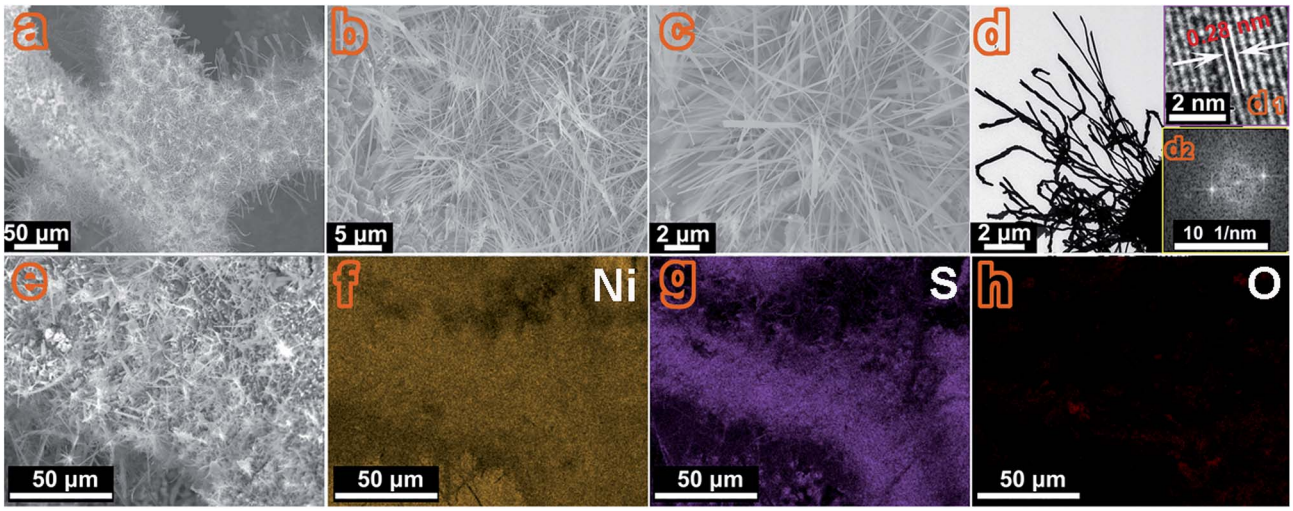

Fig. 2 (a–c) Typical SEM images of NF-4-S at different magnifications. (d) TEM image of NF-4-S, the insets are the corresponding (d1) HRTEM image and (d2) SAED patterns after FFT from Ni_3S_2 nanowires. (e–h) SEM image of NF-4-S and the corresponding EDX elemental mapping of (f) Ni, (g) S, (h) O.

of Ni_3S_2. It should be noted that NF-4-S and NF-6-S have very similar broadened diffraction peaks around 37° due to the overlap of NiO and Ni_3S_2 peaks. Fortunately, the retained Ni in all samples can act as a highly conductive scaffold and play an important role in improving the electron transfer rate.

XPS was conducted to further determine the surface components of the as-prepared NF-4-S. As displayed in Fig. 3b, no other elemental peaks were observed apart from the peaks of Ni, S, C, and O in the survey spectrum, indicating that the samples were pure. The Ni 2p spectrum (Fig. 3c) displayed two spin–orbit

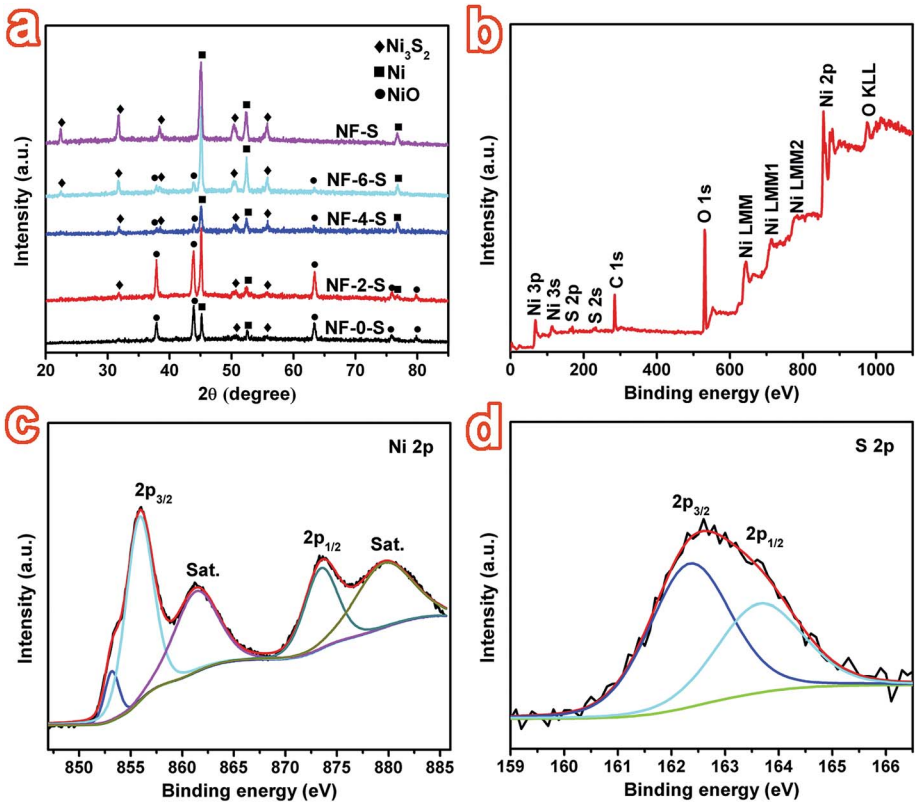

Fig. 3 (a) XRD patterns of NF-0-S, NF-2-S, NF-4-S, NF-6-S and NF-S. (b)–(d) XPS spectra of NF-4-S: (b) survey spectrum, (c) Ni 2p spectrum, and (d) S 2p spectrum.

Published on 04 April 2016. Downloaded on 25/05/2016 13:06:36.

doublet peaks at 855.8 (Ni $2p_{3/2}$) and 873.4 eV (Ni $2p_{1/2}$). The corresponding satellite peaks at 861.3 and 879.5 eV were also identified, which indicated the presence of nickel–oxygen species on the surface of NF.[46] It should be noted that a peak at 853.1 eV appears near Ni $2p_{3/2}$, corresponding to the characteristic peak of Ni_3S_2.[4,13,47] Moreover, the binding energy of 162.6 eV in Fig. 3d can be attributed to the S 2p spectrum. The fitting peak at around 162.3 eV belongs to S $2p_{3/2}$, and the peak at 163.6 eV can be assigned to S $2p_{1/2}$. These values correlate with previously reported data.[20,35] The XPS results coincide with those of the XRD patterns, confirming the presence of NiO and Ni_3S_2.

To visually observe the morphological evolution of the final product, the SEM measurements of NF-S, NF-6-S, NF-2-S and NF-0-S were also carried out. The corresponding investigation is shown in Fig. 4. Interestingly, for all samples, we could see that plenty of Ni_3S_2 nanocrystallines with different morphologies and microstructures are well adhered to the NF substrate. In detail, NF-S is densely covered by a layer of Ni_3S_2 nanocrystallines with an uneven surface, as displayed in Fig. 4a1–a3. Additionally, there are messy nanowires and rough nanorods that are entangled and conglutinated. The SEM images of NF-6-S show that highly dense short nanorods and block particles grow vertically on the surface of NF. Meanwhile, we can clearly find flower-shaped hierarchical dendrites supported on the NF surface with sporadic distribution, which are predominantly composed of irregular particles (Fig. 4b1–b3). For NF-2-S, some thin nanoflakes with extremely low density are observed (Fig. 4c1–c3). They tend to grow starting from the same center to generate an almost vertically aligned 3D architecture. However, in exposed regions, we also notice that the NF skeleton is tightly and totally covered with large and ruleless NiO/Ni_3S_2 nanosheets or blocks, forming a very uneven surface. This is similar to the observation of NF-0-S, as indicated in Fig. 4d1–d3.

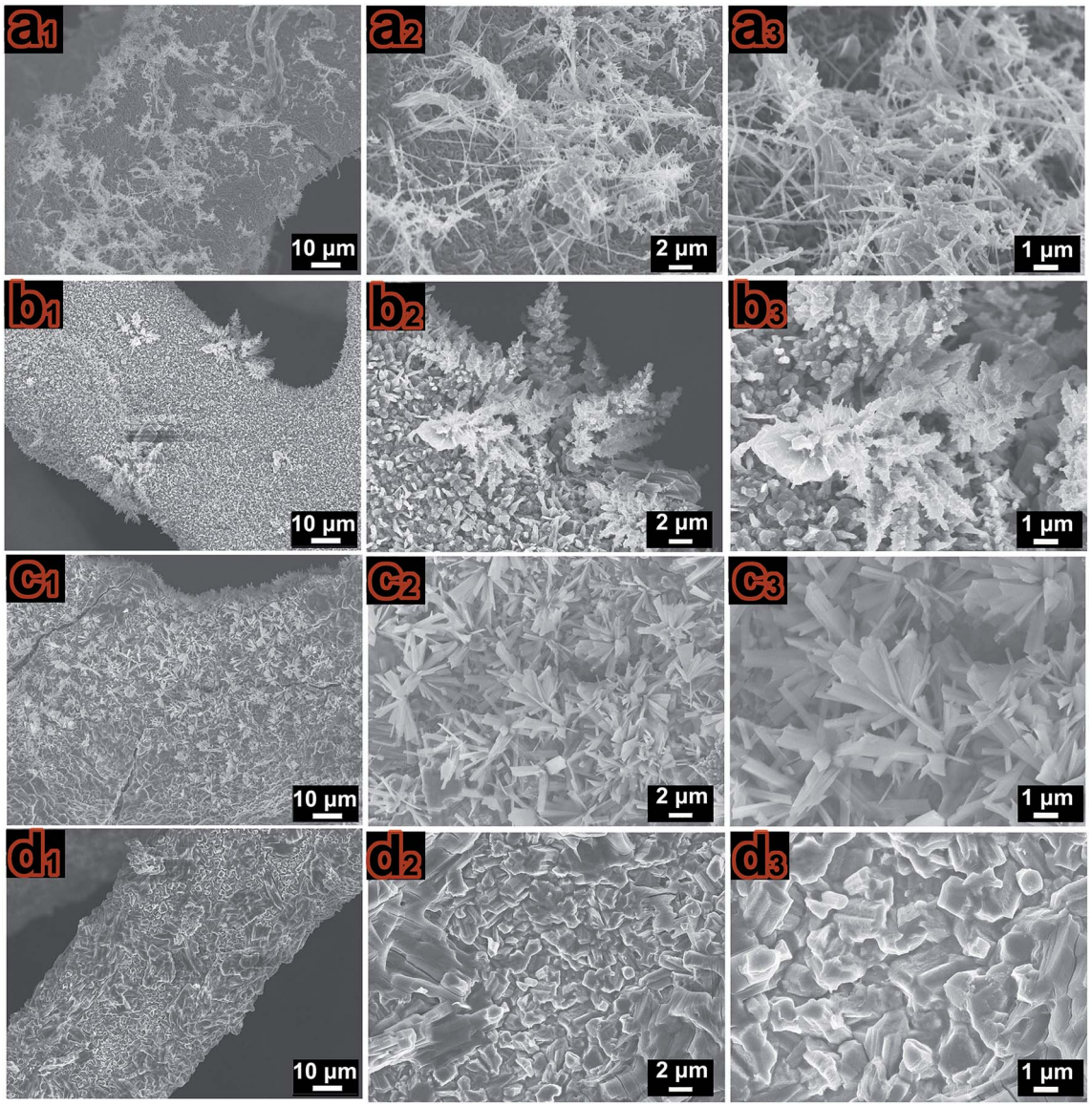

Fig. 4 Typical SEM images of (a1–a3) NF-S, (b1–b3) NF-6-S, (c1–c3) NF-2-S and (d1–d3) NF-0-S at different magnifications.

This journal is © The Royal Society of Chemistry 2016

Published on 04 April 2016. Downloaded on 25/05/2016 13:06:36.

Hydrothermal treatment resulted in a highly densely packed NiO/Ni_3S_2 hybrid layer over the entire NF surface, differing from that of the pristine oxidized sample. The surface becomes rougher than the pre-forms. This is mainly due to the anion-exchange reaction between O^{2-} and S^{2-} during the hydrothermal process, and thus a portion of NiO could be converted into Ni_3S_2.[12,37] Nevertheless, the ion exchange reaction cannot dramatically change the original architecture of NiO.[48] Consequently, we conclude that these vertically oriented Ni_3S_2 arrays are derived from the reaction between the remaining Ni and S^{2-} in solution, consistent with a previous report in the literature.[45] Compared to other samples, the vertically aligned nanostructured Ni_3S_2 arrays disappeared on the NF-0-S surface due to severe oxidation, which further confirmed the above inference. The involved chemical reaction equations can be expressed as follows:[20,34]

$$(NH_2)_2CS + 2H_2O \rightarrow H_2S + CO_2 + 2NH_3 \quad (1)$$

$$2H_2S + 3Ni \rightarrow Ni_3S_2 + 2H_2 \quad (2)$$

Because of the different oxidation degrees, we finally obtained active Ni_3S_2 arrays with a variety of morphologies supported on NF substrates. The integrated formation procedure is illustrated in Fig. 5, which includes two steps of oxidation and sulfidation. On the basis of the experimental results, a possible growth mechanism could be proposed to illustrate the formation procedure of Ni_3S_2 arrays. During the reaction, the sulfide source will be released from TAA, which can come into contact with both the surface and interior of the NF backbone by diffusion. Due to the slower diffusion rate of O^{2-}, the sulfidation rate of NiO is lower than that of Ni.[49] The released sulfide ions would firstly react with exposed Ni to generate Ni_3S_2 nuclei. In the initial stages, the low oxidation degree leads to relatively more nucleation. Then, Ni_3S_2 nuclei aggregate to assemble along their preferential orientation. Owing to the inadequate Ni content, elongated growth along the direction of (110) is favored, forming grass-like Ni_3S_2 nanorod/nanowire arrays. With further decrease of oxidation degree, more Ni located on the surface can directly react with sulfur ions to generate a dense short nanorod array, and even give rise to irregular branches. However, for the samples with a high oxidation degree, the subsequent Ni_3S_2 nanoparticles transformed from numerous NiO can adhere to the adjacent Ni_3S_2 nanocrystals, which are driven by a complex oriented attachment process. To reduce the surface energy, they join at a planar interface to form thin nanoflakes. The nucleation growth process of Ni_3S_2 arrays was affected by the content and distribution of Ni. In our experiments, the partially oxidized NF acts as the backbone to guide the nucleation of Ni_3S_2 nanocrystals during hydrothermal processes. The different nanostructures would result in different number of exposed active sites that are effective for pseudo-capacitive reaction.

From the above results, we can draw the following conclusions. Firstly, although no additives were used, Ni_3S_2 arrays perpendicularly grown on the NF surface with various morphologies were successfully prepared, confirming the reliability of the present method. Secondly, the formation of the Ni_3S_2 array structure strongly depends on the pre-oxidation degree of NF. The Ni_3S_2 arrays were scarcer when the oxidation was more severe. Finally, it is apparent that the well-defined nanorod/nanowire arrays can be fabricated on a large scale *via* appropriate regulation of the oxidation degree of NF. The exquisite design and unique nanostructural features endow our hybrid material with favourable properties for further applications.

3.2 Electrochemical performance study

In addition to the shape-controlled growth of Ni_3S_2 arrays, the oxidation degree also affects the electrochemical performance of the as-obtained electrode materials. The electrochemical

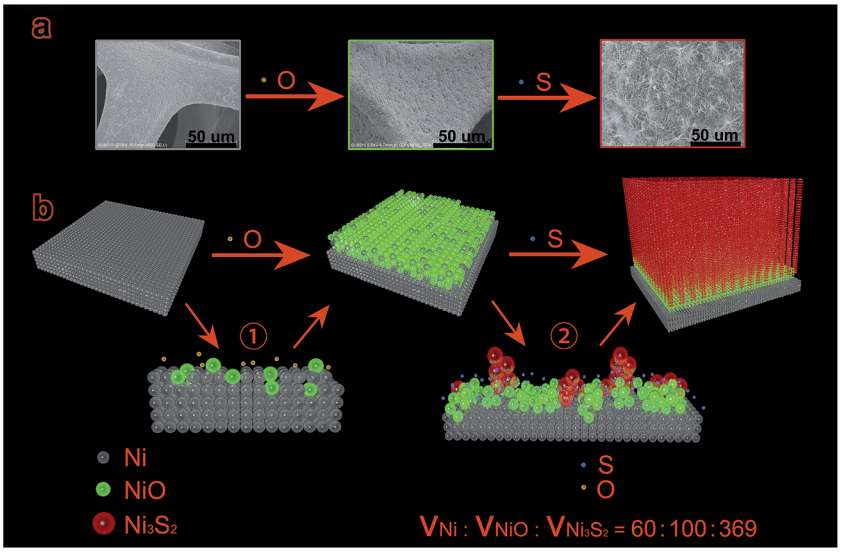

Fig. 5 Schematic illustration for the formation procedure of Ni_3S_2 arrays supported on pre-oxidized NF.

Published on 04 April 2016. Downloaded on 25/05/2016 13:06:36.

behavior of the sulfurized samples was first evaluated using CV and GCD techniques. As shown in Fig. 6a, all CV curves exhibit a pair of redox peaks, indicating a typical pseudocapacitive behavior.[34,37,45] A couple of redox peaks for Ni_3S_2 can be attributed to the reversible redox reactions of Ni^{2+}/Ni^{3+} as shown below:[18,21]

$$Ni_3S_2 + 3OH^- \leftrightarrow Ni_3S_2(OH)_3 + 3e^- \quad (3)$$

In order to clarify the real contribution to the capacitance, the pure and partial oxidation of NF was also evaluated using CV tests. Fig. S2a† shows the CV curves of pure NF and NF-*x*

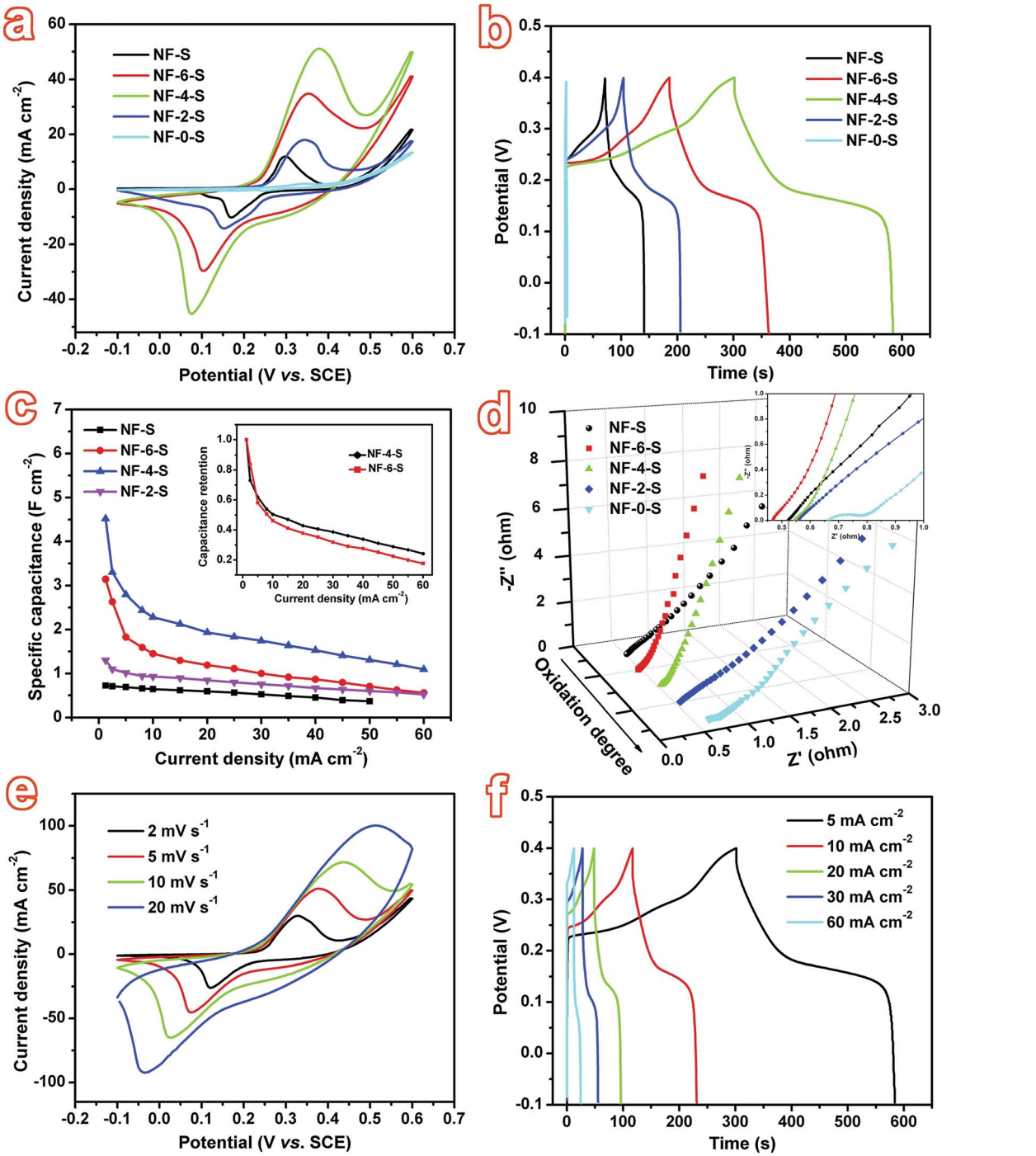

Fig. 6 Electrochemical performances of the NF-S, NF-6-S, NF-4-S, NF-2-S and NF-0-S electrodes. (a) CV curves at a scan rate of 5 mV s^{-1}, (b) GCD curves at a current density of 5 mA cm^{-2}. (c) Current density dependence of the areal capacitance for NF-S, NF-6-S, NF-4-S, and NF-2-S electrodes (inset: capacitance retention rate of NF-6-S and NF-4-S electrodes). (d) The 3d EIS spectra of the NF-S, NF-6-S, NF-4-S, NF-2-S and NF-0-S electrodes with different oxidation degrees, the insets are the partially enlarged Nyquist plots at high frequency. (e) CV curves of the NF-4-S electrode at different scan rates. (f) GCD curves of the NF-4-S electrode at different current densities.

 This journal is © The Royal Society of Chemistry 2016

Published on 04 April 2016. Downloaded on 25/05/2016 13:06:36.

electrodes at a scan rate of 5 mV s^{-1}. Evidently, the CV integrated area of the oxidized NF is close to that of pure NF, which is negligible as compared with Ni_3S_2 based electrodes. Therefore, we can infer that high temperature generated NiO provides almost no capacitance contribution to the areal capacitance due to the poor electron conductivity and greatly weakens the capacity of NiO.[25] By comparison, the enclosed area of NF-4-S is much larger than that of other electrodes, indicating a largely enhanced areal capacitance. In theory, high mass loading of active materials can produce high areal specific capacitance values. Actually, the utilization efficiency of the active materials is an important factor that affects the capacitive performance. Therefore, the hierarchical nanorod/nanowire arrays with a large accessible area can introduce more sites for the faradaic reactions, this endowed the NF-4-S electrode with excellent specific capacitance.[34,37,50] For the NF-0-S, excessive oxidation consumes a large amount of nickel and leads to the formation of a thick NiO layer, both of which hinder the generation of Ni_3S_2 arrays, accordingly, the capacitive behavior becomes worse.

Fig. 6b shows the GCD curves of the sulfurized samples with a current density of 5 mA cm^{-2}. The observed nonlinear GCD curves verify the pseudo-capacitance nature, which is well consistent with the CV curve. Compared with pure NF and NF-*x* (Fig. S2b†), the as-prepared sulfurized electrodes show much longer discharging time, indicating that the Ni_3S_2 based electrodes have higher specific capacitance, in good agreement with the CV results. Among all tested samples, NF-4-S exhibits the longest discharge time and highest specific capacitance. The specific capacitances derived from the discharge plots at different current densities were calculated (Fig. 6c), which also indicated the significantly enhanced supercapacitive performance of NF-4-S compared with other electrodes. Interestingly, the capacitances of NF-2-S, NF-4-S and NF-6-S are higher than that of NF-S, this proved that it is a promising strategy to optimize the electrochemical properties of the active Ni_3S_2 electrode by controlling the oxidation degree of the NF substrate. Besides the NF-4-S electrode, NF-6-S shows relatively higher specific areal capacitance compared with NF-S and NF-2-S electrodes. It is mainly due to the higher loading of electroactive Ni_3S_2 arrays which can be verified from its morphology. As shown in Fig. 6c, the areal capacitances decrease with increase in current density. This is mainly due to that the high scan rate limits the migration of the electrolytic ions. This makes inner active surface areas inaccessible for charge storage.[4,51] Specifically, the areal capacitances of the NF-4-S electrode were calculated to be 4.52, 3.30, 2.80, 2.28, 1.94 and 1.74 F cm^{-2} at the current densities of 1.25, 2.5, 5, 10, 20 and 30 mA cm^{-2}, respectively. The specific capacitances were 1051, 767, 651, 530, 451 and 405 F g^{-1} at the corresponding current densities mentioned above. Besides, with the charging–discharging rate increasing from 2.5 to 30 mA cm^{-2}, the NF-4-S electrode shows ~47% capacity loss, which is much smaller than the ~62% capacity loss of NF-6-S (inset). The above results demonstrate that the NF-4-S electrode has high specific capacitance and excellent rate behavior.

The superior electrochemical property of the as-prepared electrodes was further confirmed by the long-term cycling test at a current density of 20 mA cm^{-2} (Fig. S3†). For all samples, the areal capacitances slightly increase with cycling perhaps due to the self-activation process, corresponding to the redox reaction of the active species with the alkaline electrolyte.[30] A similar phenomenon was also observed for the pure NF electrode (Fig. S4†). During the cycling, the areal capacitance of the NF-4-S electrode is always higher than that of other electrodes. Especially, after 2000 continuous cycles, the specific areal capacitance of 2.13 F cm^{-2} (108.3% of the initial capacitance) for NF-4-S can be well maintained with a slight increase, demonstrating the excellent long-term stability. To the best of our knowledge, the electrochemical performance of NF-4-S obtained here is superior or comparable to the relevant data for nickel sulfide[23,32,52,53] and hybrid nickel/cobalt sulfide[54–56] nanocomposites reported in the literature (Table S1†).

EIS was further applied to evaluate the electrochemical performance. The Nyquist plots of all sulfide electrodes are illustrated in Fig. 6d, with an enlarged view at high frequency (inset). All samples demonstrate similar spectra with a semicircle at high frequency and a straight line at low frequency. NF-4-S and NF-6-S show larger slopes in the low frequency regions indicating better capacitive behavior with lower diffusion resistance.[33] These results suggest that our binder-free electrodes show excellent pseudocapacitive behavior. At high frequency, the intersection of the plot at the real part represents the equivalent series resistance (R_s), and the diameter of the semicircle corresponds to the charge transfer resistance (R_{ct}).[3,23] The R_s of NF-0-S (0.66 Ω) is significantly greater than those of the other samples (~0.5 Ω), indicating that the direct growth of vertical Ni_3S_2 arrays from the NF current collector assures quick electron transport to improve the capacitance performance. By comparison, it can be clearly observed that NF-6-S and NF-4-S exhibit lower R_{ct}, indicating their better electrical conductivity. This was probably due to that the well-defined Ni_3S_2 arrays effectively facilitate electrolyte diffusion, improving ion-transport kinetics. As expected, the electrochemical performance of the electrodes is greatly influenced by the morphology and distribution of supported active Ni_3S_2 arrays.

Furthermore, we have also evaluated the typical CV measurements of the NF-4-S electrode at different scan rates (Fig. 6e). With the increase of scan rate from 2 to 20 mV s^{-1}, the current increases accordingly and the shape of the CV curves is well maintained, implying the suitability of the NF-4-S electrode for ultrafast redox reactions. The corresponding GCD tests at various current densities were carried out in the voltage range between −0.1 and 0.4 V, as shown in Fig. 6f. The symmetric nature of GCD curves implies good electrochemical capacitive characteristics and excellent reversible redox reactions.[12] On the basis of the above analysis, NF-4-S shows the best electrochemical properties. Thus, the synergetic contribution from the pseudocapacitive materials of Ni_3S_2 together with the superiorities of the 3D hierarchical nanorod/nanowire array architecture should account for the superior electrochemical performance of the NF-4-S electrode.

To further demonstrate the actual application of the NF-4-S electrode, we constructed a 4 cm^2 asymmetric supercapacitor device using NF-4-S as the positive electrode and NPGC film on

Published on 04 April 2016. Downloaded on 25/05/2016 13:06:36.

NF as the negative electrode in 3 M KOH electrolyte with one piece of cellulose paper as the separator (denoted as NF-4-S//NPGC). The electrochemical properties of the NPGC electrode in a three-electrode system are displayed in Fig. S5.† Notably, thanks to the high specific surface area and porosity (Fig. S6†), the NPGC electrode exhibits excellent energy storage performance. For comparison, the NF-4-S and NPGC electrodes are firstly tested in a three-electrode cell with a potential window from −0.1 to 0.6 V and −1.2 to 0 V, respectively (Fig. 7a). It is noted that these two electrodes demonstrate good compatibility to assemble an asymmetric supercapacitor. Fig. S7† shows the CV curves of the asymmetric supercapacitor cell at different voltage windows with a scan rate of 20 mV s^{-1}. As expected, the stable operating voltage can be extended to 1.8 V. CV curves of the supercapacitor device at different scan rates are shown in Fig. 7b, which exhibit the typical features of both electric double-layer capacitance and pseudocapacitance in the entire potential range of 0–1.8 V. Besides, the discharge curves of the NF-4-S//NPGC supercapacitor at various current densities are also illustrated in Fig. 7c. Unlike the three electrode cell, the discharge curves of the NF-4-S//NPGC supercapacitor exhibits nearly linear variation in the full operating voltage with different current densities. This demonstrates ideal capacitive characteristics and fast charge/discharge behavior.[57] The capacitance of the full device measured at various current densities (based on the total mass of active materials in both electrodes) is calculated to further demonstrate the corresponding rate capability. As shown in Fig. 7d, under a current density of 2.5 mA cm^{-2}, the specific capacitance reaches 100.1 F g^{-1}. Even at current densities as high as 25 and 50 mA cm^{-2}, our supercapacitor is still able to deliver capacitance values of 68.4 and 50.9 F g^{-1}, respectively. These are much higher than previously reported values for the C/$CoNi_3O_4$//AC supercapacitor (~64.7 F g^{-1} at 1 mA cm^{-2}),[57] Co_3O_4@$Ni(OH)_2$//AC cell (47.6 F g^{-1} at 25 mA cm^{-2}), Co_3O_4@$Ni(OH)_2$//RGO device (49.7 F g^{-1} at 25 mA cm^{-2}),[58] and so on. Such high specific capacitance and excellent rate behavior can be attributed to the unique 3D nanorod/nanowire array structure with a large active surface area to promote fast electron transport and ion diffusion.[45]

The cycling performance test over the assembled supercapacitor at a current density of 40 mA cm^{-2} was performed using the GCD technique (Fig. 7e). As can be seen, the supercapacitor exhibits excellent long-term stability with high capacitance retention of 93.1% even after 5000 charge/discharge cycles.

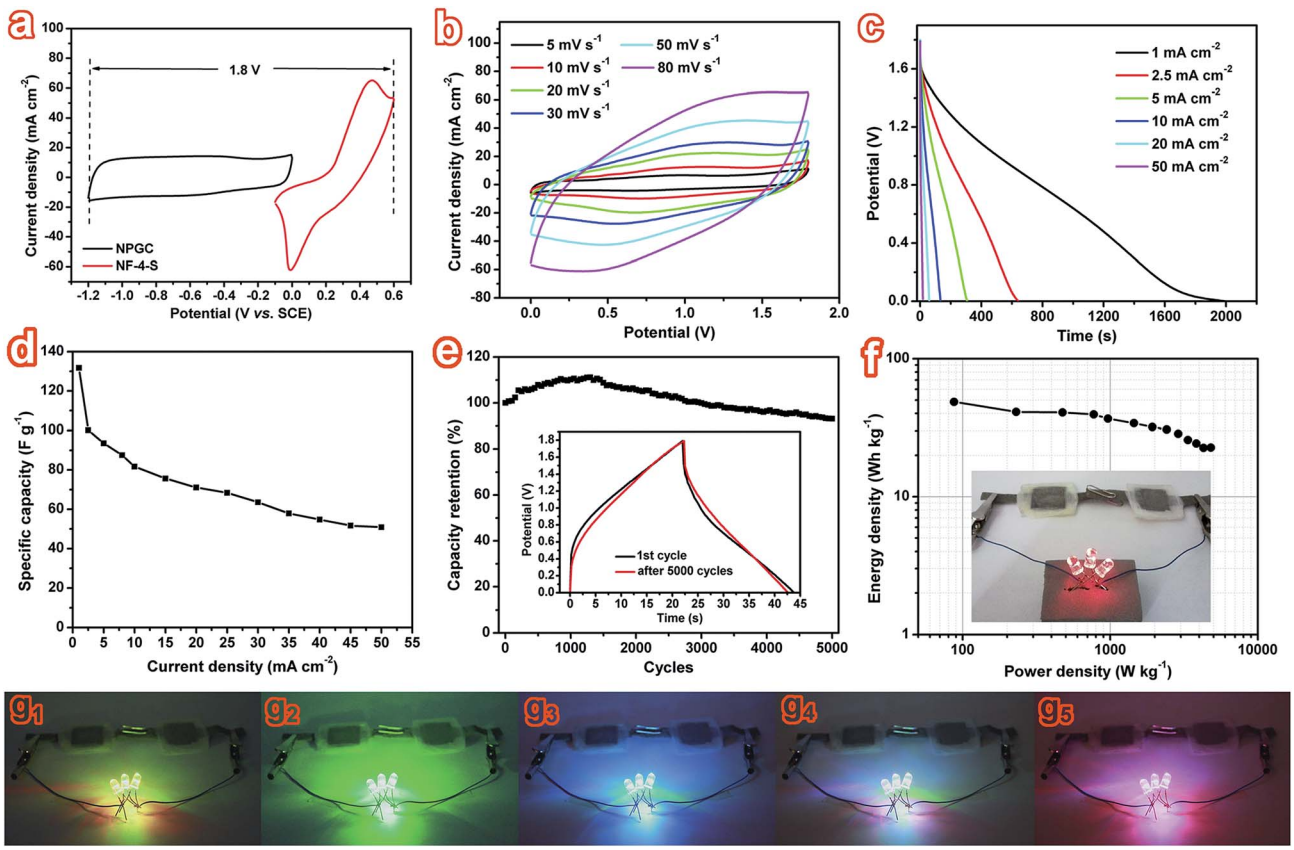

Fig. 7 (a) CV curves of NF-4-S and NPGC electrodes at a scan rate of 10 mV s^{-1} performed in a three-electrode cell. (b) CV curves of a NF-4-S//NPGC asymmetric supercapacitor measured in a voltage window of 0–1.8 V at different scan rates in 3 M KOH electrolyte. (c) Discharge curves of the asymmetric supercapacitor at different current densities. (d) Specific capacitance at different current densities for the asymmetric supercapacitor. (e) Cycle performance of the NF-4-S//NPGC supercapacitor at a current density of 40 mA cm^{-2}. Inset: charge/discharge curves of the first and the 5000th cycle. (f) Ragone plot of the supercapacitor device. Inset: optical image of two supercapacitors in series lighting up three color-changing LED indicators. (g1–g5) Color variation of the three LED indicators.

 This journal is © The Royal Society of Chemistry 2016

Published on 04 April 2016. Downloaded on 25/05/2016 13:06:36.

The remarkable cycling stability is also confirmed by the almost overlapping charge/discharge curves between the first and the 5000th cycles (Fig. 7e, inset). The capacitance increase during the first 1400 cycles is likely due to an activation process.[30] The subsequent capacity decay is probably due to the structural breakdown of the electrode material by the fast and long term cycling tests.[26] These results further verify the great potentiality of NF-4-S as an efficient supercapacitor material with high specific capacitance and good cycling stability. Besides, a Ragone plot (energy density *vs.* power density) of our NF-4-S//NPGC supercapacitor is presented in Fig. 7f. Impressively, our device shows a very high energy density of 48.5 W h kg^{-1} at a power density of 87.4 W kg^{-1} and still maintains an energy density of 28.5 W h kg^{-1} at a high power density of 2.9 kW kg^{-1}. Even at a higher power density of 4.8 kW kg^{-1}, the device still has an energy density of 22.7 W h kg^{-1}. The energy density and power density demonstrated here outperform the values reported for other asymmetric supercapacitors, including fiber-shaped all-solid-state MnO_2/carbon fiber//graphene/carbon fiber ASCs (27.2 W h kg^{-1} at 979.7 W kg^{-1}),[10] Co_3O_4@$Ni(OH)_2$//AC (41.83 W h kg^{-1} at 33.46 W kg^{-1}), Co_3O_4@$Ni(OH)_2$//RGO (41.90 W h kg^{-1} at 36.10 W kg^{-1}),[58] Ni–Co sulfide nanowires//activated carbon cells (25 W h kg^{-1} at 447 W kg^{-1})[37] and V_2O_5–ECF//ECF device (22.3 W h kg^{-1} at 1500 W kg^{-1}).[9] Accordingly, two identical asymmetric cells separately charged to 1.8 V at 8 mA cm^{-2} connected in series can easily illuminate three color-changing LED indicators (Fig. 7g1–g5). The inset in Fig. 7f shows the brightness of the three LED indicators after being lit up for 10 min. Specifically, the red light can glow for more than 35 min. The above evidence convincingly demonstrates the great potential of our supercapacitor device for practical applications.

4. Conclusions

In summary, we report a novel and effective strategy for controlled building of 3D hierarchical Ni_3S_2 arrays grown directly on NF with various morphologies, and were applied as binder-free supercapacitor electrodes. A two-step synthesis approach was exploited based on simple high temperature annealing of NF precursors and subsequent hydrothermal reaction. By appropriately adjusting the pre-oxidation degree of the NF substrate, well-defined grass-like Ni_3S_2 nanorod/nanowire arrays perpendicularly oriented on NF (NF-4-S) can be obtained. Such a unique structural design effectively improved ion/charge transportation along active Ni_3S_2 nanorods/nanowires to NF, and greatly increased the active area. Consequently, the NF-4-S electrode delivered an extremely high specific areal capacitance of 4.52 F cm^{-2} at a current density of 1.25 mA cm^{-2}, as well as good rate capability and long cycle stability. A corresponding asymmetric supercapacitor was assembled which possessed a high energy density of 48.5 W h kg^{-1} at a power density of 87.4 W kg^{-1}. Our supercapacitor device also exhibited remarkable cycling stability with capacitance retention of 93.1% after 5000 cycles. More significantly, this study provides a novel perspective for the controllable architectural design of nickel sulfide electrodes. The present strategy could also be applied to create other composite materials with desirable nanostructures for advanced energy storage applications.

Acknowledgements

The authors gratefully acknowledge the financial support for this research from the National Natural Science Foundation of China (21375043, 21175051).

References

1 P. Simon and Y. Gogotsi, *Nat. Mater.*, 2008, **7**, 845–854.
2 Q. Lu, J. G. Chen and J. Q. Xiao, *Angew. Chem., Int. Ed.*, 2013, **52**, 1882–1889.
3 C. Zhou, Y. Zhang, Y. Li and J. Liu, *Nano Lett.*, 2013, **13**, 2078–2085.
4 H. B. Li, M. H. Yu, F. X. Wang, P. Liu, Y. Liang, J. Xiao, C. X. Wang, Y. X. Tong and G. W. Yang, *Nat. Commun.*, 2013, **4**, 1894–1900.
5 P. Simon, Y. Gogotsi and B. Dunn, *Science*, 2014, **343**, 1210–1211.
6 L. Q. Mai, A. Minhas-Khan, X. Tian, K. M. Hercule, Y. L. Zhao, X. Lin and X. Xu, *Nat. Commun.*, 2013, **4**, 2923–2929.
7 Y. Cheng, H. Zhang, C. V. Varanasi and J. Liu, *Energy Environ. Sci.*, 2013, **6**, 3314–3321.
8 F. Bonaccorso, L. Colombo, G. Yu, M. Stoller, V. Tozzini, A. C. Ferrari and V. Pellegrini, *Science*, 2015, **347**, 1–9.
9 L. Li, S. Peng, H. B. Wu, L. Yu, S. Madhavi and X. W. Lou, *Adv. Energy Mater.*, 2015, **5**, 1500753.
10 N. Yu, H. Yin, W. Zhang, Y. Liu, Z. Tang and M. Q. Zhu, *Adv. Energy Mater.*, 2015, **6**, 1501458.
11 D. P. Dubal, P. Gomez-Romero, B. R. Sankapal and R. Holze, *Nano Energy*, 2015, **11**, 377–399.
12 W. Hu, R. Chen, W. Xie, L. Zou, N. Qin and D. Bao, *ACS Appl. Mater. Interfaces*, 2014, **6**, 19318–19326.
13 W. Wei, L. Mi, Y. Gao, Z. Zheng, W. Chen and X. Guan, *Chem. Mater.*, 2014, **26**, 3418–3426.
14 L. Shen, L. Yu, H. B. Wu, X. Y. Yu, X. Zhang and X. W. Lou, *Nat. Commun.*, 2015, **6**, 6694–6701.
15 X. Liu, S. Shi, Q. Xiong, L. Li, Y. Zhang, H. Tang, C. Gu, X. Wang and J. Tu, *ACS Appl. Mater. Interfaces*, 2013, **5**, 8790–8795.
16 X. Y. Yu, L. Yu, H. B. Wu and X. W. Lou, *Angew. Chem., Int. Ed.*, 2015, **54**, 5331–5335.
17 X. Y. Yu, L. Yu and X. W. Lou, *Adv. Energy Mater.*, 2016, **6**, 1501333.
18 H. Huo, Y. Zhao and C. Xu, *J. Mater. Chem. A*, 2014, **2**, 15111–15117.
19 J. M. Falkowski, N. M. Concannon, B. Yan and Y. Surendranath, *J. Am. Chem. Soc.*, 2015, **137**, 7978–7981.
20 L. L. Feng, G. Yu, Y. Wu, G. D. Li, H. Li, Y. Sun, T. Asefa, W. Chen and X. Zou, *J. Am. Chem. Soc.*, 2015, **137**, 14023–14026.
21 J. Wang, S. Wang, Z. Huang and Y. Yu, *J. Mater. Chem. A*, 2014, **2**, 17595–17601.
22 T. Zhu, H. B. Wu, Y. Wang, R. Xu and X. W. Lou, *Adv. Energy Mater.*, 2012, **2**, 1497–1502.

Published on 04 April 2016. Downloaded on 25/05/2016 13:06:36.

23 D. Kong, C. Cheng, Y. Wang, J. I. Wong, Y. Yang and H. Y. Yang, *J. Mater. Chem. A*, 2015, **3**, 16150–16161.
24 S. I. Kim, P. Thiyagarajan and J. H. Jang, *Nanoscale*, 2014, **6**, 11646–11652.
25 Y. Gao, L. Mi, W. Wei, S. Cui, Z. Zheng, H. Hou and W. Chen, *ACS Appl. Mater. Interfaces*, 2015, **7**, 4311–4319.
26 M. Shao, Z. Li, R. Zhang, F. Ning, M. Wei, D. G. Evans and X. Duan, *Small*, 2015, **11**, 3530–3538.
27 R. B. Rakhi, W. Chen, D. Cha and H. N. Alshareef, *Nano Lett.*, 2012, **12**, 2559–2567.
28 J. Wang, X. Zhang, Q. Wei, H. Lv, Y. Tian, Z. Tong, X. Liu, J. Hao, H. Qu, J. Zhao, Y. Li and L. Mai, *Nano Energy*, 2016, **19**, 222–233.
29 X. Cai, R. V. Hansen, L. Zhang, B. Li, C. K. Poh, S. H. Lim, L. Chen, J. Yang, L. Lai, J. Lin and Z. Shen, *J. Mater. Chem. A*, 2015, **3**, 22043–22052.
30 L. Wan, J. Xiao, F. Xiao and S. Wang, *ACS Appl. Mater. Interfaces*, 2014, **6**, 7735–7742.
31 Y. Ai, X. Geng, Z. Lou, Z. M. Wang and G. Shen, *ACS Appl. Mater. Interfaces*, 2015, **7**, 24204–24211.
32 Z. Zhang, Z. Huang, L. Ren, Y. Shen and X. Qi, *Electrochim. Acta*, 2014, **149**, 316–323.
33 Y. Ruan, J. Jiang, H. Wan, X. Ji, L. Miao, L. Peng, B. Zhang, L. Lv and J. Liu, *J. Power Sources*, 2016, **301**, 122–130.
34 J. Wang, D. Chao, J. Liu, L. Li, L. Lai, J. Lin and Z. Shen, *Nano Energy*, 2014, **7**, 151–160.
35 Y. Liao, K. Pan, Q. Pan, G. Wang, W. Zhou and H. Fu, *Nanoscale*, 2015, **7**, 1623–1626.
36 G. Yang, H. Han, T. Li and C. Du, *Carbon*, 2012, **50**, 3753–3765.
37 Y. Li, L. Cao, L. Qiao, M. Zhou, Y. Yang, P. Xiao and Y. Zhang, *J. Mater. Chem. A*, 2014, **2**, 6540–6548.
38 C. Wang, D. Wang, Q. Wang and H. Chen, *J. Power Sources*, 2010, **195**, 7432–7437.
39 H. W. Liang, S. Liu, J. Y. Gong, S. B. Wang, L. Wang and S. H. Yu, *Adv. Mater.*, 2009, **21**, 1850–1854.
40 H. Zhou, Y. Wang, R. He, F. Yu, J. Sun, F. Wang, Y. Lan, Z. Ren and S. Chen, *Nano Energy*, 2016, **20**, 29–36.
41 W. Ni, B. Wang, J. Cheng, X. Li, Q. Guan, G. Gu and L. Huang, *Nanoscale*, 2014, **6**, 2618–2623.
42 J. G. Railsback, A. C. Johnston-Peck, J. Wang and J. B. Tracy, *ACS Nano*, 2010, **4**, 1913–1920.
43 S. Ci, Z. Wen, Y. Qian, S. Mao, S. Cui and J. Chen, *Sci. Rep.*, 2015, **5**, 1–12.
44 N. A. Kyerematen, C. Lebouin, P. Knauth and T. Djenizian, *Electrochim. Acta*, 2013, **88**, 814–820.
45 W. Zhou, X. Cao, Z. Zeng, W. Shi, Y. Zhu, Q. Yan, H. Liu, J. Wang and H. Zhang, *Energy Environ. Sci.*, 2013, **6**, 2216–2221.
46 W. Zhou, X. J. Wu, X. Cao, X. Huang, C. Tan, J. Tian, H. Liu, J. Wang and H. Zhang, *Energy Environ. Sci.*, 2013, **6**, 2921–2924.
47 P. Hu, T. Wang, J. Zhao, C. Zhang, J. Ma, H. Du, X. Wang and G. Cui, *ACS Appl. Mater. Interfaces*, 2015, **7**, 26396–26399.
48 X. Xia, C. V Zhu, J. Luo, Z. Zeng, C. Guan, C. F. Ng, H. Zhang and H. J. Fan, *Small*, 2014, **10**, 766–773.
49 P. J. Mangnus, E. K. Poels, A. D. Van Langeveld and J. A. Moulijn, *J. Catal.*, 1992, **137**, 92–101.
50 G. Zhang, T. Wang, X. Yu, H. Zhang, H. Duan and B. Lu, *Nano Energy*, 2013, **2**, 586–594.
51 X. Xia, J. Tu, Y. Zhang, X. Wang, C. Gu, X. B. Zhao and H. J. Fan, *ACS Nano*, 2012, **6**, 5531–5538.
52 S. W. Chou and J. Y. Lin, *J. Electrochem. Soc.*, 2013, **160**, D178–D182.
53 L. Yu, B. Yang, Q. Liu, J. Liu, X. Wang, D. Song, J. Wang and X. Jing, *J. Electroanal. Chem.*, 2015, **739**, 156–163.
54 W. Kong, C. Lu, W. Zhang, J. Pu and Z. Wang, *J. Mater. Chem. A*, 2015, **3**, 12452–12460.
55 M. Sun, J. Tie, G. Cheng, T. Lin, S. Peng, F. Deng, F. Ye and L. Yu, *J. Mater. Chem. A*, 2015, **3**, 1730–1736.
56 H. Wan, J. Jiang, J. Yu, K. Xu, L. Miao, L. Zhang, H. Chen and Y. Ruan, *CrystEngComm*, 2013, **15**, 7649–7651.
57 J. Zhu, J. Jiang, Z. Sun, J. Luo, Z. Fan, X. Huang, H. Zhang and T. Yu, *Small*, 2014, **10**, 2937–2945.
58 C. H. Tang, X. Yin and H. Gong, *ACS Appl. Mater. Interfaces*, 2013, **5**, 10574–10582.

This journal is © The Royal Society of Chemistry 2016